J. Fluid Mech. (2007), *vol.* 586, *pp.* 397–422. © 2007 Cambridge University Press
doi:10.1017/S0022112007006891 Printed in the United Kingdom

Experimental observations of the merger of co-rotating wake vortices

T. BERTÉNYI AND W. R. GRAHAM

Department of Engineering, University of Cambridge,
Trumpington Street, Cambridge CB2 1PZ, UK

(Received 16 August 2005 and in revised form 22 April 2007)

The interaction and merger of a pair of co-rotating vortices has been studied experimentally in a wind tunnel. The vortices are generated using two separate wings, allowing both initial circulation ratio and initial separation to be varied. At the nominal test speed of $30\,\mathrm{m\,s^{-1}}$, the circulation-based Reynolds number is typically 6.4×10^4. Mean crossflow velocities at stations downstream are obtained with a traverse-mounted yaw meter. The vortex interaction is characterized by fitting Lamb–Oseen profiles to the measured, azimuthally averaged, tangential velocity profiles.

It is found that the merger process differs in several important respects from lower-Reynolds-number studies. First, the separation of the vortices decreases continually throughout the initial, 'viscous growth', phase, instead of remaining constant. Second, the vortex core growth in this phase appears to be greater than can be accounted for by turbulent diffusivity, even after correcting for the effects of wandering. Finally, the time to merger lies well below that predicted by expressions based on the lower-Reynolds-number observations, and is further reduced when the circulation ratio departs from unity. We conclude that the enhanced core growth is probably due to the short-wavelength 'elliptic' instability that has already been observed in some high-Reynolds-number experiments. The mechanism behind the decrease in separation, which is a crucial factor in the reduced merger time, is three-dimensional, but, beyond this, remains unknown.

1. Introduction

A body which moves through a fluid and generates a force normal to the free-stream direction will shed a vortical wake. In the context of aircraft, this results in the well-known trailing vortex pair, often visible as a 'contrail'. A following aircraft flying into the vortices will experience significant, and potentially disastrous, changes in altitude (Crouch 2005). Thus the frequency with which aircraft can use the busiest airports is in large part limited by the requirement to avoid such an encounter by maintaining a safe separation. Unsurprisingly then, there are significant motivations to reassess the separation criteria, but to do so safely requires a deeper understanding of the problem than currently exists. (For reviews of research to date see Spalart 1998 or Rossow 1999.)

An essential starting point is the ability to predict trailing vortex topology far downstream. A simplified trailing vortex pair model, as in figure 1(*a*), is often used to describe this structure. In fact, this is a reasonable approximation only for cruise conditions, when the hazard is not a serious concern. A more realistic wake is shown in figure 1(*b*); a vortex is shed wherever there is an inflection point in the spanwise

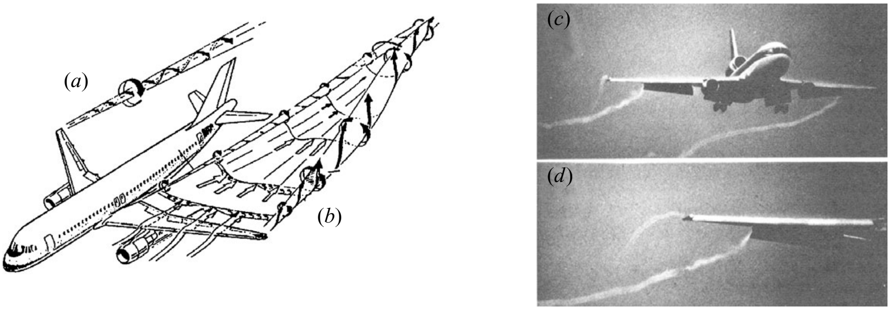

FIGURE 1. Illustrations of the character of aircraft trailing wake vortices. The idealization of a single trailing tip vortex (*a*) gives way to the more realistic description of a vortex sheet shed from the wing, (*b*). This sheet typically rolls up into coherent vortex structures. During high-lift configurations, this typically means two co-rotating vortices per wing, from the tip and the outboard flap, (*c*) and (*d*) Burnham & Sullivan (1973).

lift distribution curve. On a modern wing operating in high-lift configuration, this includes the wing tips, flap and control surface edges, engine nacelles, and the body. Vortices can also be shed from the empennage. Most of these smaller vortices roll up together quite rapidly. However, it is usual for the two strongest – from the wing tip and the outboard flap – to survive this process. (Figures 1(*c*) and 1(*d*) show these vortices in conditions sufficiently humid for condensation to render them visible.) When (if) they merge, and how they do so, is an important issue in the determination of an aircraft's far-field wake.

Numerical modelling of wake vortex merger is arduous, as it requires a fine spatial resolution in the crossflow plane and a very long domain in the streamwise direction. To date, we are aware of no fully three-dimensional numerical studies of this problem (though Czech *et al.* 2005 have successfully simulated wind-tunnel-scale experiments with a parabolized, Reynolds-averaged Navier–Stokes code). A closely related and much more tractable topic is the merger of co-rotating two-dimensional vortices (see for example Jimenez, Moffatt & Vasco 1996) and it has consequently given rise to a sizeable body of work. For a pair of identical, inviscid, two-dimensional co-rotating vortices there is an initial separation, d_0, beyond which they never merge. Viscous vortices starting in this regime initially maintain a constant separation, but growth of the core radius, r_c, serves to decrease the normalized separation, d_0/r_c, over a time proportional to the flow Reynolds number (Meunier, Le Dizès & Leweke 2005; note, however, that Huang 2005 has queried the universality of this scaling). Once this diffusion phase brings the pair of vortices to a critical normalized separation, the cores start to interact directly and merger occurs. Numerical predictions by Christiansen (1973), Rossow (1977), and Melander, Zabusky & McWilliams (1988) suggest that the critical value is $d_0/r_c \approx 3.4$. Subsequent experimental investigations by Meunier *et al.* (2002) have confirmed these predictions. (Related work by Meunier & Leweke 2005, however, shows evidence of three-dimensional instability during the merger of two-dimensional vortices at higher Reynolds numbers, and this short-wave, or 'elliptic', instability has now also been successfully described theoretically by Le Dizès & Laporte 2002 and Bristol *et al.* 2004.)

In practice, of course, the case of identical vortices is rather singular. Dritschel & Waugh (1992) thus simulated the interaction of two patches of equal, uniform vorticity but differing radii. A much richer range of qualitative behaviour was observed, even for small changes in radius ratio. This feature may, however, be an artefact of the vorticity distribution chosen, as more recent computations by Trieling, Velasco Fuentes & van Heijst (2005) with continuous distributions show features closer to the equal vortex case. Where both works agree is in the prediction of 'straining out' of the weaker vortex around the stronger when the inequality is significant.

The first attempt to characterize the merger of trailing vortices experimentally was by Brandt & Iversen (1977). They argued that the distance to merger, d_m, should depend on the vortex circulations, Γ_{01} and Γ_{02}, core sizes, r_{c1} and r_{c2}, initial separation, d_0, and the free-stream velocity, U. They further suggested that the process could be regarded as quasi-two-dimensional, and thereby replaced d_m with an equivalent time, $t_m = d_m/U$. Then, on dimensional grounds,

$$t_m = \frac{d_0^2}{\Gamma_{01}} f\left(\frac{\Gamma_{01}}{\Gamma_{02}}, \frac{r_{c1}}{r_{c2}}, \frac{d_0}{r_c}\right). \tag{1.1}$$

Although their experimental observations were restricted to flow visualization, the results supported a relationship of this form. Strangely, however, the span and chord of the wings used to generate the vortices were introduced to non-dimensionalize their data, so one cannot deduce the specific form of equation (1.1) that is implied. Other contemporary wind tunnel test results (e.g. Corsiglia, Rossow & Ciffone 1976 and some of the work summarized by Rossow 1999) are similarly restricted to qualitative data. Attempts at measuring wake vortices in flight tests have also been made (Iversen 1976; Gardoz & Clawson 1993; Roberts, Vicroy & Smith 2000) but, while they have the advantage of realistic conditions and full-scale (circulation-based) Reynolds number, $Re_\Gamma = \Gamma_0/\nu$, they have again been compromised by lack of, or uncertainties in, quantitative data.

Among more recent laboratory studies, we have already noted that Meunier *et al.*'s (2002) two-dimensional experiments agree with the numericists' view of merger. This picture is also supported by Cerretelli & Williamson (2003), whose towing tank study used two cambered-plate wings to generate a pair of trailing vortices. They identified a Reynolds-number-dependent diffusive phase, with core sizes growing while the vortices orbit at constant separation, a merger phase consisting largely of convective behaviour but completed by axisymmetrization in a 'second diffusive stage', and finally a merged diffusive phase. This description was found to apply equally to laminar ($Re_\Gamma < 530$) and turbulent ($853 < Re_\Gamma < 1665$) vortices, as long as a turbulent diffusivity and a different convective merger time were employed in the latter case. The laminar merger times also showed good quantitative agreement with Meunier *et al.*'s results (for laminar vortices with $700 < Re_\Gamma < 2300$). No turbulent vortex data at comparable Reynolds numbers are available elsewhere; however, we note that a change in (dimensionless) convective merger time seems to contradict the idea of a phase which is independent of diffusive effects. Additionally, the proposed expression significantly over-predicts the data of Chen, Jacob & Savas (1999), obtained from towing tank studies of flapped, cambered-plate wings. They find a dimensionless time to merger around 0.8 for a wide range of flap/tip vortex circulation ratios at Reynolds numbers $Re_\Gamma \approx 5 \times 10^4$. In contrast, Cerretelli & Williamson's convective phase alone lasts 0.81 dimensionless time units, and their overall prediction would be roughly double this value. Chen *et al.*'s work also shows an important qualitative difference in the first diffusive phase, in that separation distance starts to decrease as soon as the vortices are formed, well before the onset of the merger phase. From consideration of the evolution of the vorticity field variance (and higher-order moments), Chen *et al.* infer significant three-dimensional activity throughout their experiments; however, similar short-term variations in the moments also appear in the field of the isolated tip vortex shed by a flap-less wing, so it is unclear whether these particular fluctuations can be linked to merger. Furthermore, once all the flow vorticity is captured in the measurement window, the moments never increase in the long term, and the decreases seen could perhaps be due to diffusive effects. Unfortunately, no data for core size evolution are given in the paper, so the significance of such effects is not known.

More concrete evidence of three-dimensionality during merger is found in the experiments of Bristol, Ortega & Savaş (2003). Here flow visualizations clearly show the presence of the short-wave instability that Meunier & Leweke (2005) observed at their highest Reynolds number. On the basis of these results, Jacquin *et al.* (2005) attribute high-Reynolds-number vortex merger exclusively to this mechanism. While this assertion perhaps requires further supporting evidence, it does seem that extension of the low-Reynolds-number description to the high-Reynolds-number case via a turbulent diffusivity is an oversimplification.

In summary, then, high-Reynolds-number ($Re_\Gamma \sim 10^5$) results appear to show departures from the consensus view of vortex merger that has been developed on the basis of experiments and simulations at $Re_\Gamma \sim 10^3$. Apart from the implication of three-dimensional instability in the merger phase, there are also important discrepancies in the initial, co-rotating phase. Specifically, Chen *et al.*'s (1999) measurements suggest that it is shorter than the diffusive model would predict, and is no longer characterized by constant vortex centre separation. However, the use of flapped wings introduces the additional (albeit more realistic) complications of a wake generated by a single wing lift distribution: differing circulations and core sizes, a connecting vortex sheet, and an imposed strain field due to the vortices on the other side of the symmetry plane. Devenport, Vogel & Zsoldos (1999) have conducted experiments at similar Reynolds numbers with vortices generated by separate wing tips, but they were more interested in turbulence characteristics pre- and post-merger, and hence took measurements at only a few crossflow planes. (They did, however, observe a 25% reduction in separation during the pre-merger orbital phase.) Further data from this type of configuration and Reynolds number range seem called for. The object of this work is therefore to revisit Brandt & Iversen's (1977) experiment in a quantitative, and more extensive, manner. We also seek to extend the results to the case of vortices with differing circulations.

The structure of the paper is as follows. In § 2 we describe our experimental apparatus (including the rotary yaw meter used to measure wake velocities), and the calculation of vortex characteristics derivable from the velocity field. The downstream evolution of these characteristics in the merger of equal-strength vortices is discussed in § 3. The extent to which this behaviour is modified by inequality in vortex circulations is then described in § 4. The implications for the role of three-dimensionality are addressed specifically in § 5, and the overall conclusions of the study are summarized in § 6.

2. Experimental apparatus and data analysis

The vortex interaction was studied in a wind tunnel. The tip vortices shed from two lifting wings were measured using a single-tube yaw meter mounted on a two-axis crossflow plane traverse. The longitudinal position of the traverse was fixed, and the vortex-generating wings were shifted longitudinally in one-chord increments to study the streamwise development of the interaction. Finer variations in streamwise location were achieved by moving the yawmeter in its mounting. The overall experimental arrangement is shown in figure 2.

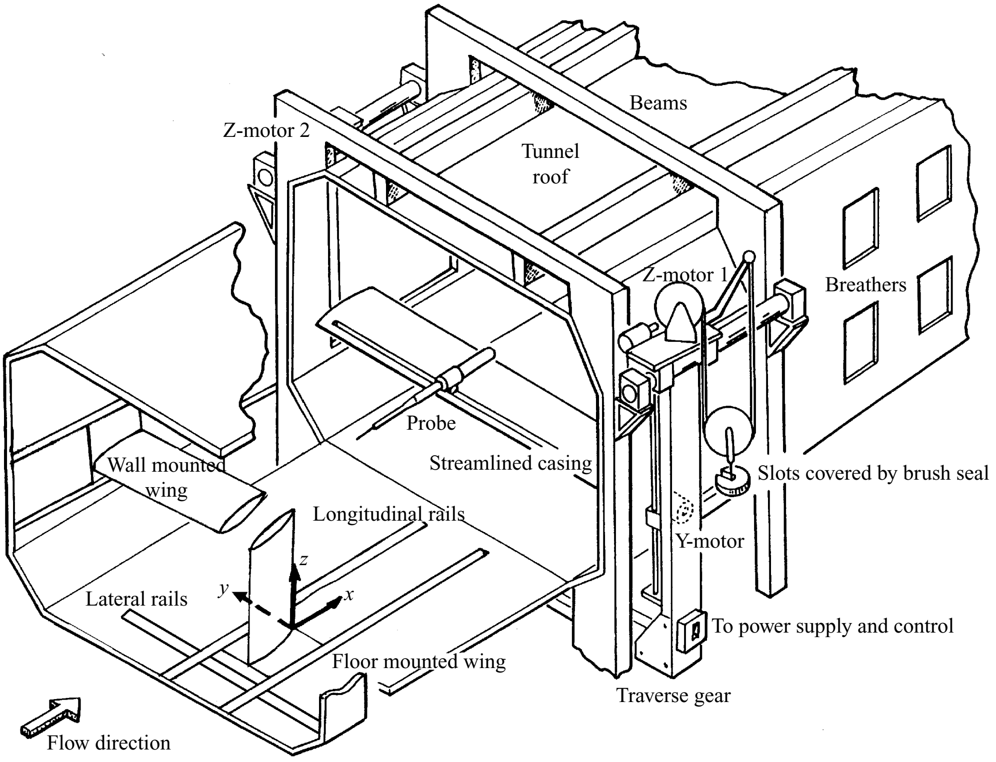

FIGURE 2. Sketch illustrating the general arrangement of the experimental apparatus. The vortex-generating wings are arranged for the nominally equal case presented in § 3.2.

The closed-circuit, low-speed wind tunnel has a test section which is 1.68 m wide by 1.22 m high and – in the current configuration – has a usable length of 2.8 m. Tapered chamfer sections are used to prevent a longitudinal pressure gradient due to wall boundary-layer growth. The empty tunnel turbulence intensity was measured to be 0.15% at the test condition of 30 m s^{-1}. The coordinate system is depicted in figure 2; the origin is fixed at the centreline of the tunnel floor, level with the trailing edge of the wings.

The vortices were generated using two identical NACA0012 section wings with a constant chord of 0.152 m and a semispan aspect ratio of 5 (i.e. effective aspect ratio 10). Large endplates were fitted to avoid interference from the tunnel wall boundary layer. The flat end-cap NACA0012 was chosen because the trailing vortex it sheds is well-documented (see for example Brandt & Iversen 1977; Dacles-Mariani *et al.* 1995; Devenport *et al.* 1996, 1999) and it has been reported to roll up very quickly into a tight coherent vortex (see for example Ramaprian & Zheng 1997; Anderson *et al.* 2001; Spall 2001). The relative position and angle of attack of the wings could be adjusted independently in discrete steps (for repeatability), allowing variations in both initial vortex separation and relative strength. The typical resulting vortex had a core radius of approximately 10 mm and a circulation of around $-1.0\,\mathrm{m}^2\,\mathrm{s}^{-1}$, resulting in a circulation-based Reynolds number of 6.4×10^4.

A single-tube rotary yaw meter – broadly similar to the Chu-Tube (Chu *et al.* 1987) – was designed and implemented (see Bertényi 2001 for details). This device is similar to a five-hole probe, but with a single chamfered tube rotated through four

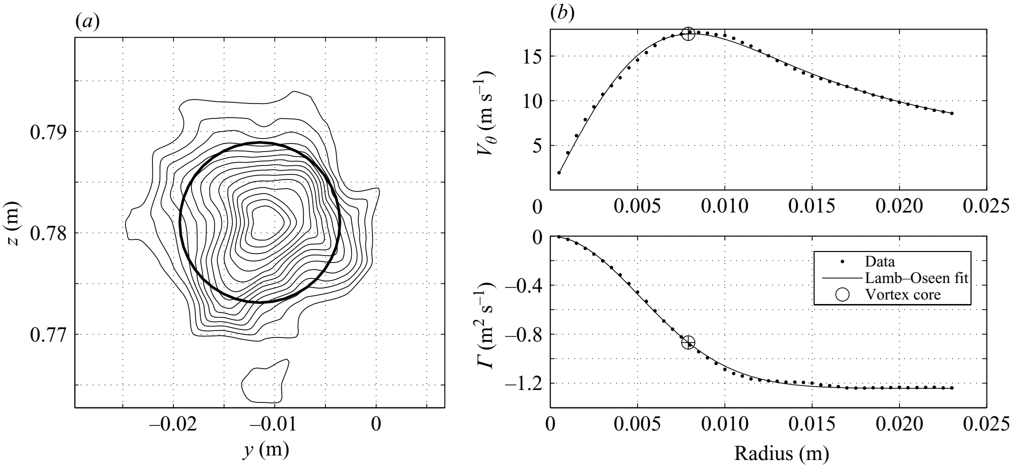

FIGURE 3. (*a*) A typical experimentally measured vortex depicted as contours of constant vorticity starting at $-500\,\mathrm{s}^{-1}$ in contour increments of −500. The circulation and azimuthally averaged tangential velocity are plotted against increasing radius in (*b*). The bold circular contour in (*a*) is that used in determining the vortex centre.

orthogonal positions and a sliding outer tube for the total pressure reading, resulting in a measurement volume under 1 mm^3. The pressure transducer was built into the probe body and the pneumatic volume was kept to a minimum in order to provide a rapid response. Probe actuation, timing, and measurement were optimized so as to complete a single measurement cycle in 760 ms.

The two-axis traverse was located at the end of the test section and driven by a DC Servo system with position feedback, providing location accuracy to within ±0.005 mm. A typical survey covered 230 mm × 230 mm with a 3 mm grid spacing, and provided both crossflow velocity components and position information. These data were numerically differentiated, using a centred-difference approximation, to estimate the streamwise vorticity, ω_x. The errors associated with this process are discussed by Graham, David & Bertényi (2004), who give the maximum absolute vorticity discrepancy as $2\sqrt{2}\Delta v_c/\Delta$, where Δv_c is the maximum crossflow velocity error (5% for our probe), and Δ the grid spacing. The uncertainty in the vorticity estimate thus varies with position, and will be discussed on a case-by-case basis.

Global measures of the vortices were determined as follows. The location was defined as the centre of an optimized circular contour, the optimum occurring when the contour was positioned to maximize its circulation. (For a purely axisymmetric vortex, this definition coincides with the peak vorticity, but this is not necessarily true for a more general structure such as the distorted vortices in the final stages before merger.) The contour radius was that corresponding to maximum azimuthally averaged tangential velocity, where measurement errors should be least significant. The circulation integral was evaluated using a trapezoidal approximation, with the required velocities obtained from the experimental data via bi-linear interpolation. A typical vortex located in this way is presented in figure 3(*a*), with the resulting circulation and average tangential velocity estimates plotted against increasing radius in figure 3(*b*). At the peak tangential velocity of approximately 18 m s^{-1}, the maximum vorticity error is about 850 s^{-1}, i.e. almost two of the contours in figure 3(*a*). Away from this radius, the value drops in proportion to the tangential velocity. Note also that the overall circulation of $1.2\,\mathrm{m^2\,s^{-1}}$ is about half of that expected at the wing root (based on lifting-line theory). This figure is supported by a two-dimensional roll-up calculation, which shows the remaining vorticity to be not yet captured at 3 chords downstream. As subsequent circulation data will show, it remains uncaptured, presumably because the dynamics become dominated by the vortex–vortex interaction.

The measured vortex structure is well-represented by the Lamb–Oseen vortex model (Saffman 1992):

$$\Gamma(r) = \Gamma_0\left(1 - \mathrm{e}^{-kr^2}\right) \tag{2.1}$$

where Γ_0 is the circulation of the vortex and k is indicative of its length scale. (The Lamb–Oseen vortex is a solution of the two-dimensional Navier–Stokes equations when $k = (4\nu(t + t_0))^{-1}$.) The point of maximum tangential velocity and hence, by definition, the vortex core radius, r_c, can be found by differentiation, giving:

$$r_c = \sqrt{\frac{1.25643}{k}}.$$

The parameters k and Γ_0 are determined by a nonlinear least-squares fit to the measured tangential velocity data. The tangential velocity was used instead of the circulation because it is weighted more towards the vortex core, where higher velocities mean the accuracy of the data is better. The quality of the fit can be characterized by the R^2 parameter, defined as one minus the ratio of the mean-squared velocity error to the mean-squared velocity (Bertényi 2001). For the data shown in figure 3(*b*), $R^2 = 0.999$. The streamwise variation of R^2 is described later.

For the vorticity field as a whole, we define the centroid of vorticity, $(\bar{Y}, \bar{Z})$, by

$$\bar{Y} = \frac{\int y\omega_x\,\mathrm{d}A}{\int \omega_x\,\mathrm{d}A}, \qquad \bar{Z} = \frac{\int z\omega_x\,\mathrm{d}A}{\int \omega_x\,\mathrm{d}A} \tag{2.2}$$

and the second moment of vorticity, or dispersion length D, by

$$D^2 = \frac{\int [(y - \bar{Y})^2 + (z - \bar{Z})^2]\omega_x\,\mathrm{d}A}{\int \omega_x\,\mathrm{d}A}. \tag{2.3}$$

These integrals were evaluated directly from the estimated vorticity field, via summation over the grid cells.

A potential problem with experimental studies of trailing vortices is vortex wandering, a slow movement of the vortex core sometimes present in wind tunnel experiments (Devenport *et al.* 1996). Green & Acosta (1991) note that this movement means that any time-averaged point measurement is actually a weighted average in both time and space, with clear ramifications for our wake survey method. Devenport *et al.* (1996) observed wandering amplitudes between 7% and 30% of the core radius, typically resulting in a 12% over-predicted core radius and a 15% under-predicted maximum tangential velocity. They also showed that with Gaussian wandering any vorticity distribution would tend to smear towards a Gaussian form. An ancillary study of wandering levels in our facility is described in Appendix B.

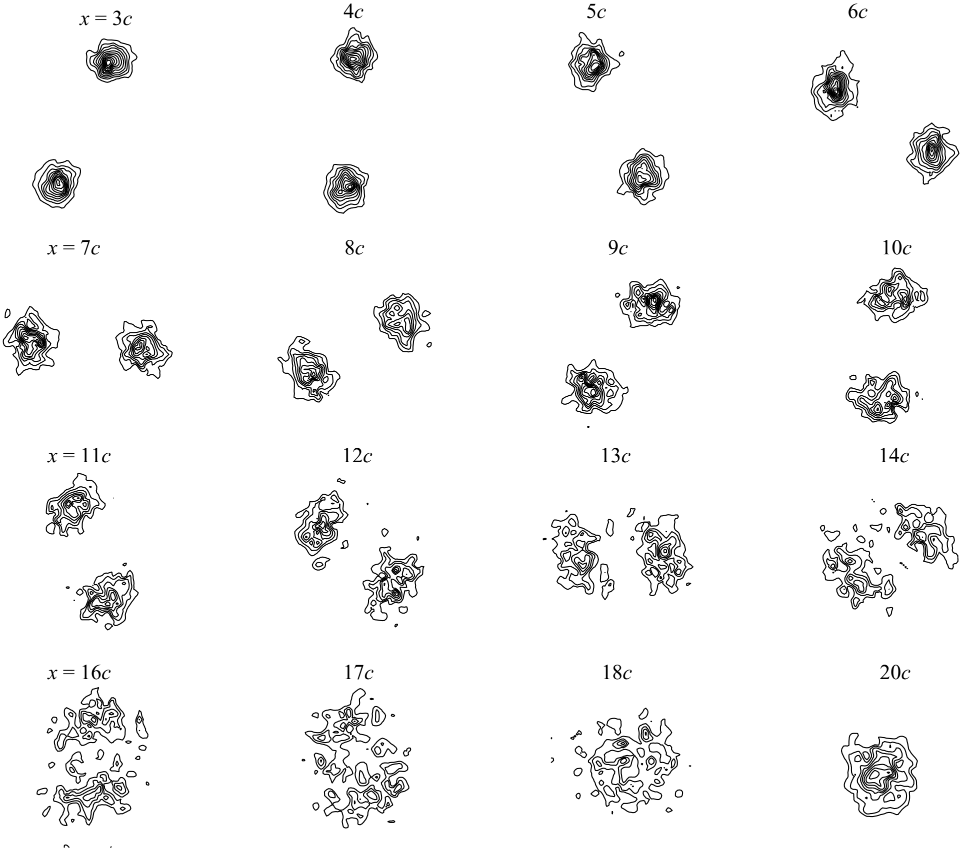

FIGURE 4. Sequence of equal vortices merging depicted using contours of streamwise vorticity, where the contour increment is $-500\,\mathrm{s}^{-1}$. The longitudinal positions of the frames are marked in chord lengths. Merger is complete by 20 chord lengths downstream.

3. Merger of equal vortices

3.1. *Physical features*

The first case studied was that of two equal vortices. The generator wings were set on opposite walls at the same angle of attack and with a fixed distance between the wing tips. Over 70 wake surveys were made at longitudinal positions from 3 to 20 chords (0.46–3.05 m) behind the wing. The results of sixteen such surveys are collated in figure 4. Note that the peak value of the maximum vorticity error (estimated from the Lamb–Oseen fit parameters) is about $670\,\mathrm{s}^{-1}$ at 3 chords and $410\,\mathrm{s}^{-1}$ at 13 chords, both of which are comparable to the contour spacing ($500\,\mathrm{s}^{-1}$).

The two vortices co-orbit in an anticlockwise direction, completing just under one and a half turns before merger. During this period the vortices draw together while simultaneously increasing in size. This growth is termed ‘vortex blooming’ since, as will be seen, it is not due to viscous diffusion. In the final stages before merger, the vortices interact strongly and their initially clear, well-defined structures show significant distortion. Once the vortices reach this final stage, merger occurs quickly.

The overall evolution can be categorized into three phases: the initial co-orbiting of the vortices ($x = 3c \rightarrow 13c$), the actual merging process ($x = 14 \rightarrow 18c$), and the merged resulting vortex ($x = 20c$ onwards). As the normalized separation approaches

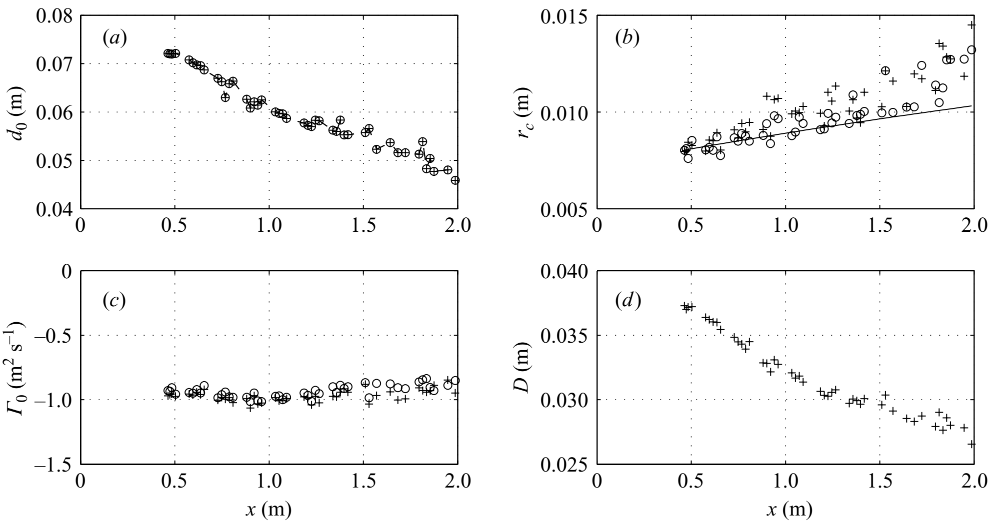

FIGURE 5. Behaviour of two equal co-rotating vortices during the initial interaction leading up to merger. Data from 3 to 13 chord lengths downstream are shown. (*a*) Decrease in separation. (*b*) Growth of vortex cores and the predicted core growth due to turbulent diffusion. (*c*) Invariance of circulation. (*d*) Decrease in dispersion length.

$d_0/r_c = 3$ (approximately corresponding to $x = 14c$), the outer fringes of the vortices start to overlap and by $d_0/r_c = 2$ (approximately corresponding to $x = 18c$) the two cores touch. Two chords further downstream, the direct interaction of the cores has resulted in a single, axisymmetric, merged vortex.

These qualitative observations are broadly similar to those reported by others. In particular, the largely undisturbed initial co-rotation accompanied by core growth, followed by significant distortion of the vortices once critical separation is reached, and subsequent rapid merger, have been observed by Devenport *et al.* (1999), Chen *et al.* (1999), Meunier & Leweke (2005) and Cerretelli & Williamson (2003). However, only the first two studies report a decrease in separation during the initial phase, while the second pair explicitly characterize it as one of constant separation. Furthermore, by the end the vortices already show significant distortion, and this distortion is oriented differently from that previously observed in the merger phase. Finally, filamentation is not unambiguously visible during merger. However, given the potential errors in the vorticity estimates, we cannot definitively say that it is not present.

Quantitative analysis of the interaction rests on the Lamb–Oseen fit described in § 2. As soon as the wake has rolled up into a coherent vortex, approximately three chord lengths behind the wing tip, the R^2 statistic is typically 0.99 or better (Bertényi 2001). This strong agreement persists throughout the initial interaction. In fact, even after extensive vortex distortion, the average azimuthal velocity still displays an R^2 statistic of 0.98 or better.

The qualitative observations made previously are reinforced by the quantitative characterization. In figure 5 the separation, core radius, circulation and dispersion length of the vortices are shown up to 2 m downstream, after which the analysis method can no longer easily distinguish them. (Recall that merger occurs at 3 m downstream.)

In figure 5(*a*) the vortex separation is shown to decrease by over a third. This drawing together is approximately linear with downstream distance and hence equivalent time. Simultaneously, the vortices grow in radius. The rate is at first slow, but then accelerates as merger is approached. A Lamb–Oseen vortex is expected to grow with the square root of time, $r_c = \sqrt{4\nu(t + t_0)}$, due to viscous diffusion. Spalart (1998) suggests this would be enhanced by turbulent diffusion, giving $r_c \approx \sqrt{8.2 \times 10^{-4}(t + t_0)}$ for the current configuration. The growth observed in figure 5(*b*), however, is over twice what this expression would predict: from approximately 8 mm to 12.5 mm instead of 10 mm.

The circulation of the vortices is not expected to change and figure 5(*c*) confirms that it is effectively constant. Though not shown, the merged vortex has a strength that is equal to the sum of the two constituent vortices.

Finally, the dispersion length, D, diminishes throughout the interaction (figure 5*d*). This is entirely consistent with the theoretical result for the idealized flow: $D^2 = (d_0/2)^2 + r_c^2$. Note, however, that it is not consistent with a two-dimensional flow, where D remains constant for an inviscid fluid (Batchelor 1967) and increases for a viscous one (Dritschel 1985).

3.2. *Parameterization of the merger process*

In order to parameterize the problem, it is necessary to vary the initial vortex separation. This can be achieved with the configuration illustrated in figure 2, where one wing is mounted on lateral rails on the tunnel floor. In total, seven different initial separations were studied. The slightly asymmetric flow field arising from this arrangement leads to different wing loadings. As a result, the circulation ratio between the two vortices was not exactly 1.0 but, on average, 0.92. The corresponding vortices are thus referred to as *nominally equal.*

To collapse data for the different initial separations, the progress towards merger is now represented as a function of non-dimensionalized separation, d_0/r_c. Separation decreases as merger is approached; thus the interaction progresses from right to left when presented in these terms and, in the limit as a single merged vortex results, $d_0/r_c \rightarrow 0$.

Vortex core radii for both the nominally and exactly equal data sets are shown in figure 6(*a*). For each pair of vortices, the instantaneous core radius is normalized by the core radius for that data set at $d_0/r_c = 4$. This point in the evolution was chosen as it is well into the vortex interaction, yet in a region where behaviour is still consistent across all the data sets. All the results then collapse onto a single curve despite the variations in circulation ratio and core radius. For example, at $d_0/r_c = 4$ the core radii in the data set vary from 7 mm to 14 mm. Both vortices in a pair bloom at approximately the same rate. The rate of blooming is roughly constant up to a non-dimensionalized separation of approximately $d_0/r_c = 3.4$; after this point it increases as merger is approached.

In figure 6(*b*), separation normalized on that at $d_0/r_c = 4$ is shown as a function of d_0/r_c. Again, the entire nominally equal data set collapses onto a single trend. (At $d_0/r_c = 4$ the non-normalized separations in the data set vary from 30 mm to 55 mm). Separation is thus seen to decrease throughout the entire interaction for a wide range of initial conditions, even at very large non-dimensionalized separations.

The dispersion length normalized on its value at $d_0/r_c = 4$ is shown in figure 6(*c*). Here it is clear that the direct link to separation noted in figure 5 is not sustained indefinitely. Below a non-dimensionalized separation of approximately 3.4, D remains effectively constant. These two distinct phases in the interaction – also seen in figure 6(*a*) – suggest a change in the underlying physics. Perhaps not coincidentally, it occurs at the critical separation for two-dimensional vortex merger.

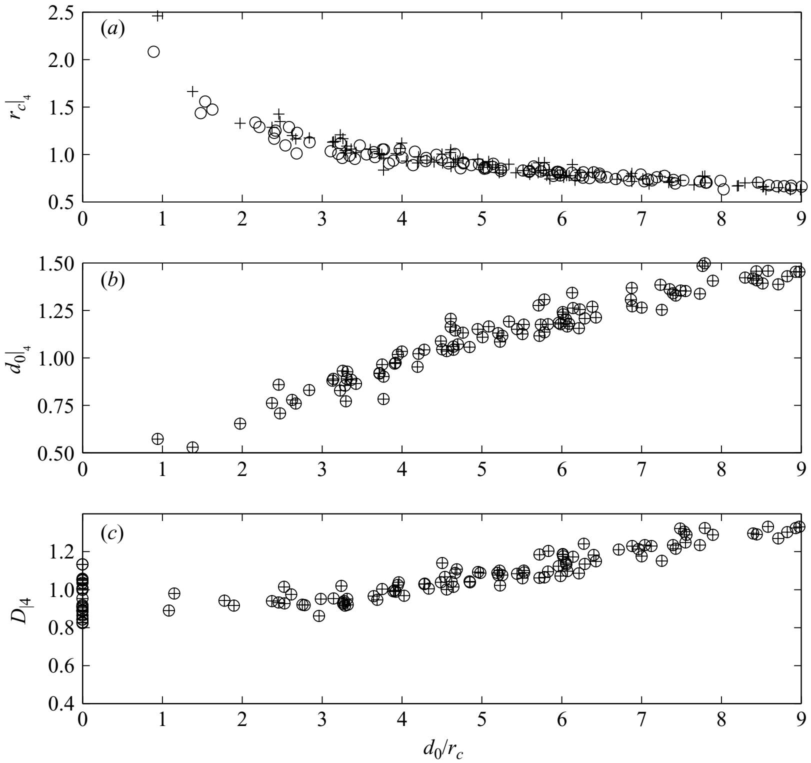

FIGURE 6. Initial interaction and co-orbiting of nominally equal vortices. The stronger vortex of the pair is indicated by +, the weaker by ○. (*a*) Blooming of the vortex cores, normalized to $d_0/r_c = 4$, (*b*) separation of the vortex cores, normalized to $d_0/r_c = 4$, and (*c*) dispersion length normalized to $d_0/r_c = 4$, all as a function of non-dimensionalized separation.

Finally, we consider the time to merger of our vortex pairs. For two identical vortices of circulation Γ_0, equation (1.1) reduces to

$$\frac{t_m \Gamma_0}{\pi d_0^2} = fn\left(\frac{d_0}{r_c}\right). \tag{3.1}$$

Incorporating a factor of π results in the time to merger being normalized by the orbital angular velocity for two point vortices, $\Omega_{pred} = \Gamma_0/\pi d_0^2$. (This observation holds for unequal vortices too, as long as Γ_0 is defined as $(\Gamma_{01} + \Gamma_{02})/2$. We thus use the latter form for the nominally equal cases.)

In principle, our experiments give only one data point for (3.1) from each wing configuration. However, the set can be greatly extended by treating each measurement plane as the source of a new value of d_0/r_c. This manoeuvre is justifiable as long as the vortices providing our new 'initial' condition remain axisymmetric, and it allows us to characterize the unknown function of equation (3.1) in much greater detail.

This non-dimensionalized time to merger for equal and nominally equal vortices is presented in figure 7(*a*). The collapse of the data is not complete. In their experiments, Chen *et al.* (1999) observed merger to occur within $0.78 \times 2\pi$ dimensionless time units. (They do not quote the corresponding d_0/r_c, but taking d_0 as roughly the distance between their wing's flap edge and tip implies a value of around 5.) This result is shown and provides reasonable agreement at separations of 5 and above.

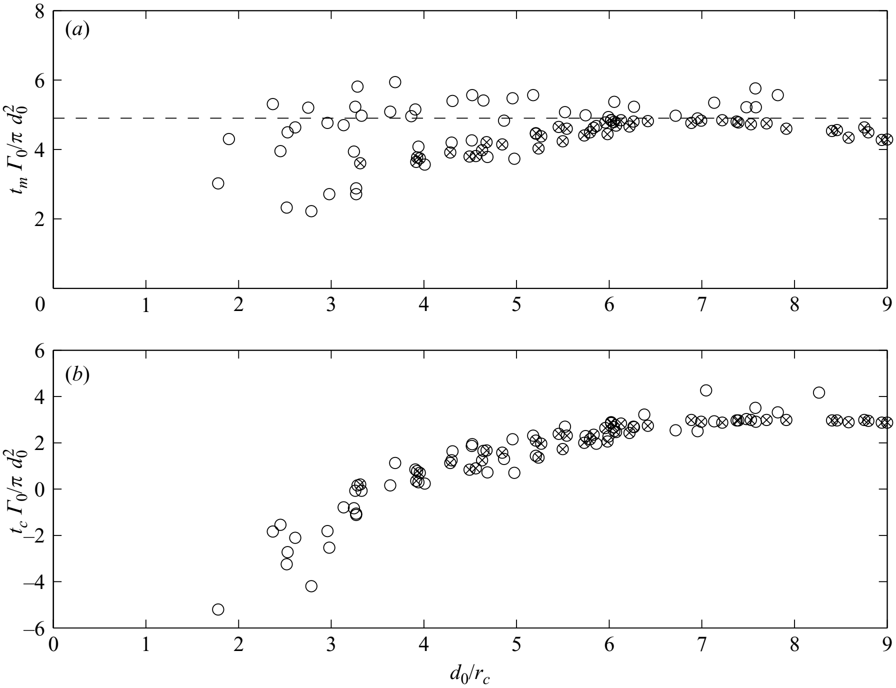

FIGURE 7. (*a*) The non-dimensionalized time to merger for equal and nominally equal vortices as a function of non-dimensionalized separation. The dashed line indicates the fit of the data of Chen *et al.* (1999). (*b*) The non-dimensionalized time to critical separation for equal and nominally equal vortices as a function of non-dimensionalized separation. Data points shown by × are from the equal data set presented in § 3.1.

However, as the overall collapse of the data is not entirely convincing we have also investigated parameterizing the interaction using the time to critical separation, defined as

$$t_c = \frac{(x_c - x)}{U_\infty}$$

where $(x_c - x)$ is the distance to the point where $d_0/r_c = 3.4$. This gives a greatly improved collapse, shown in figure 7(*b*). We hypothesize that this is linked to the increase in data scatter at small normalized separations, which could be due to a breakdown in the assumption of axisymmetry. This would then lead to variations in the convective merger time, depending on the degree of asymmetry at the critical separation.

4. Merger of unequal-strength vortices

Unequal-strength cases were generated by varying the angle of attack of the wings. Two circulation ratios were investigated: 0.477 and 0.323.

The vorticity contour plots in figure 8 depict the interaction of unequal-strength vortices with a circulation ratio of 0.477. Certain aspects are similar to the equal-strength case; throughout the initial interaction the two vortices co-orbit, draw together and show signs of blooming. A new feature, however, is the noticeable distortion of the weaker vortex during this interaction. In this sense, the interaction appears similar to the 'complete straining out' regime originally identified by Dritschel & Waugh (1992).

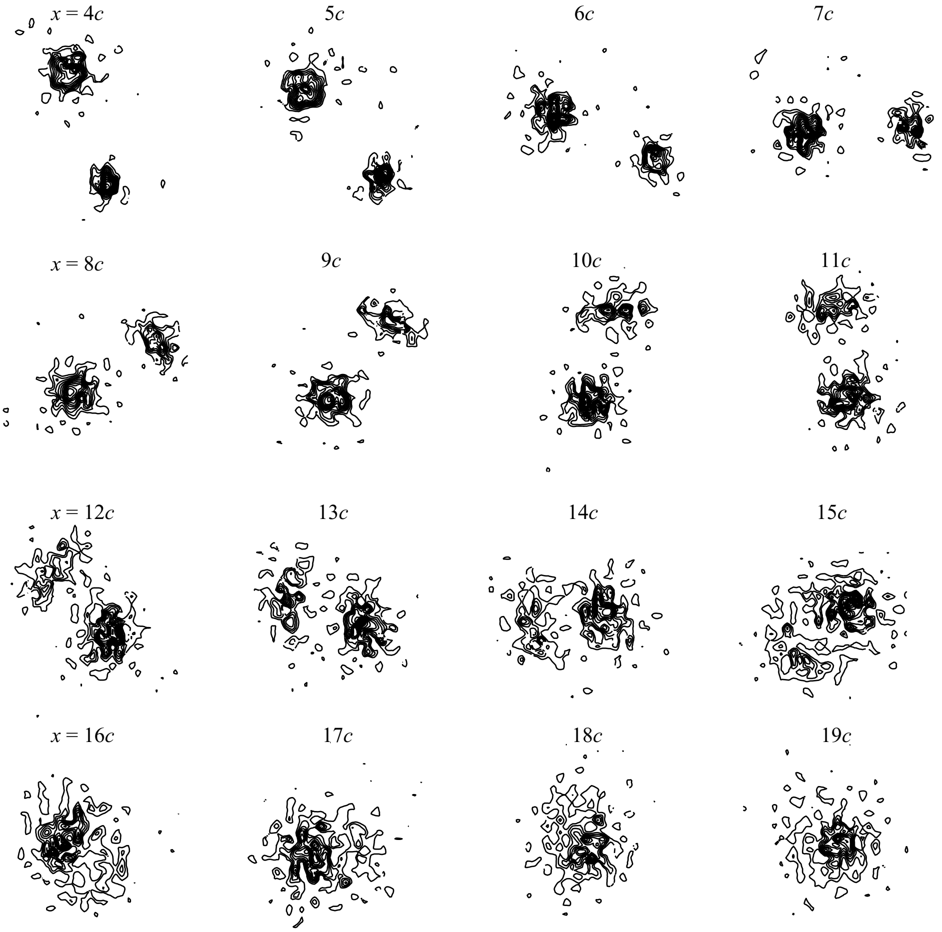

FIGURE 8. Sequence of unequal-strength vortices merging, depicted using contours of constant vorticity, where each contour is an increment of $-500\,\mathrm{s}^{-1}$. The circulation ratio is 0.477. The longitudinal distance between succesive frames is one chord length. Merging occurs at a downstream position of 18 chord lengths.

Note, however, that the orientation of the distorted vortices is again different to that seen in purely two-dimensional simulations. Finally, the actual merging process ($x = 16c$ to $18c$) appears to take less time than for the nominally equal vortices.

These trends extend to the more extreme circulation ratio of 0.323 (not shown). Here, the weaker vortex is so heavily distorted that it eventually appears to be almost wrapped around the stronger. However, as previously, the averaged azimuthal velocity continues to show a Lamb–Oseen profile well into the asymmetric stage.

The evolution of normalized core radius and separation for the entire unequal-strength data set is presented in figure 9, and a curve fit of the nominally equal data is also shown. The increased scatter in the data as merger is approached is a reflection of the strong distortion of the unequal-strength vortices and an elevated degree of unsteadiness. As with the equal-strength case, the successful collapse of figure 9(a) shows that the rate of blooming is a function of how close the vortices are to merging. An obvious difference, however, is that it varies between the two vortices: the weaker vortices bloom faster than the stronger vortices. For example, between a normalized

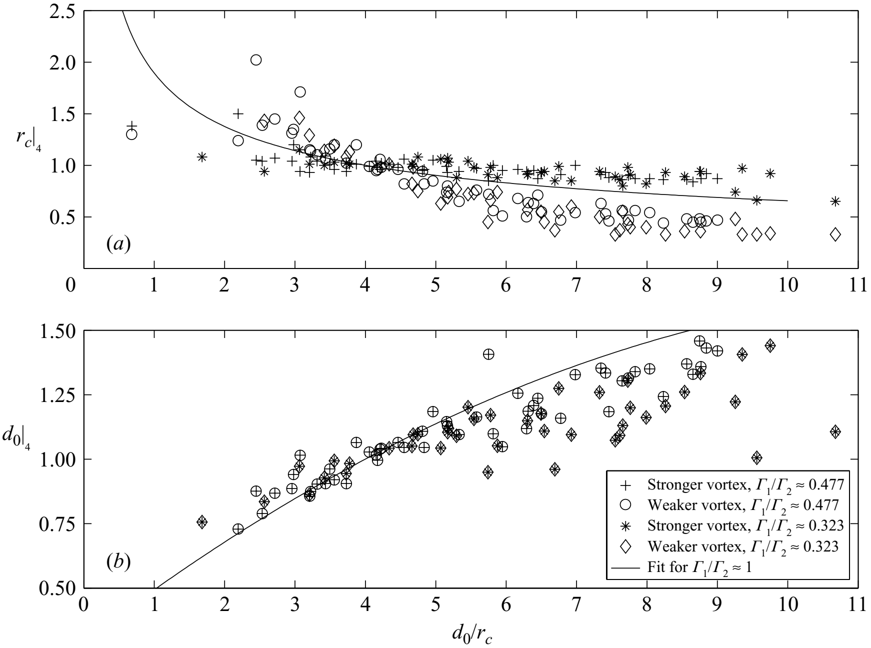

FIGURE 9. Initial interaction and co-orbiting of unequal-strength vortices. The equal-strength data set is represented by a curve-fit to the data. (*a*) Blooming of the vortex cores, normalized to d_0/r_c. (*b*) Separation of the vortex cores, normalized to $d_0/r_c = 4$.

separation of $d_0/r_c = 10$ and $d_0/r_c = 2.5$, the weaker vortices bloom from 50% of the normalized value to 150%, and the stronger from 90% to 110%. The average rate of blooming, although not shown, corresponds closely to that of the nominally equal vortices. Additionally, and unexpectedly, the collapse appears to be independent of the circulation ratio.

Separation is shown in figure 9(*b*) to decrease throughout the interaction. Up to $d_0/r_c = 5$, the unequal vortices draw together at a rate that is slightly slower than the nominally equal vortices. Also, although there is some scatter in the data, it appears that the smaller-circulation-ratio pairs have a lower rate of decrease of separation. After this point, the data sets seem to converge.

Other properties of the unequal-strength vortices behave similarly to the nominally equal case. The circulations are conserved throughout the interaction and the total circulation is present in the resulting merged vortex. The dispersion length initially decreases, though to a lesser extent than before, and then remains constant from $d_0/r_c = 3.4$ onwards.

The non-dimensionalized time to critical separation is presented in figure 10(*b*) as a function of initial separation, for both circulation ratios. The equal-strength behaviour is represented by two discontinuous curves fitted to the data before and after the critical separation. The unequal-strength vortices reach the critical separation somewhat more quickly. However, there is no clear difference between the two circulation ratios. It is also interesting to note again the collapse onto a single curve, despite the significant vortex asymmetry as the ‘initial’ conditions tend to the critical separation ratio.

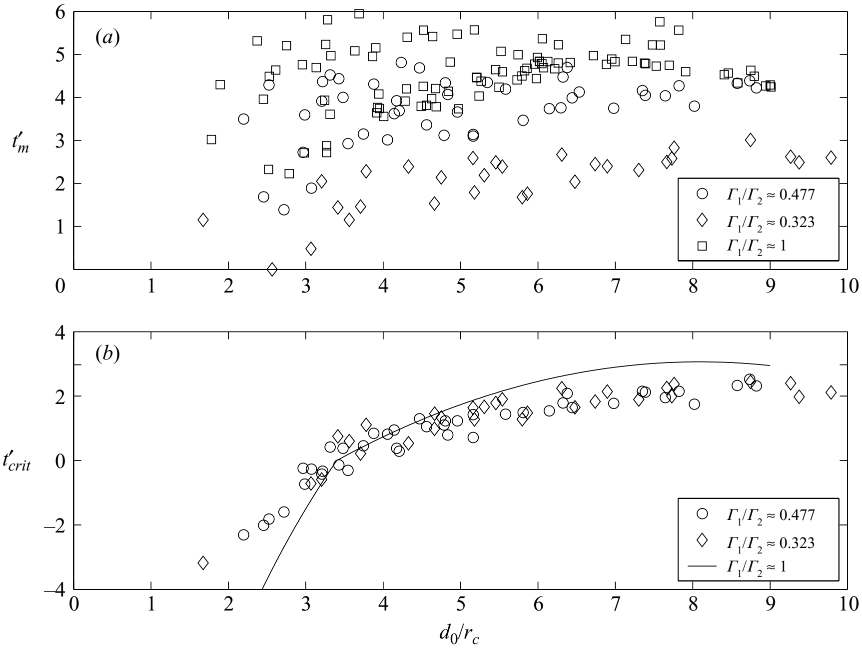

FIGURE 10. (*a*) The non-dimensionalized time to merger for equal and unequal vortices as a function of non-dimensionalized separation. (*b*) The non-dimensionalized time to critical separation for equal and nominally equal vortices as a function of non-dimensionalized separation. For clarity, the equal data set from figure 7 is represented by a curve fit.

While the time to critical separation shows a good collapse for all the data, it fails to provide information on the time for merger to occur after the critical separation is reached. Therefore, the non-dimensionalized time to merger is plotted for all three circulation ratios in figure 10(*a*). Although the collapse is less good, a clear trend is apparent; as the difference in strength between the two vortices increases, the distance to merger decreases. Two nominally equal-strength vortices will take around twice as long to merge as vortices with a circulation ratio of 0.323. This is in contrast to the conclusions of Chen *et al.* (1999) whose data show no clear effect of circulation ratio on the time to merger. However, their ratios are generally closer to one than ours; in particular they only have one case below 0.40.

5. Discussion

In discussing our results, it is first useful to summarize our qualitative findings in the light of earlier work. Most significantly, we observe a consistent and repeatable decrease in vortex separation throughout the phase from formation until critical normalized separation. This finding agrees with the experiments of Chen *et al.* (1999) and Devenport *et al.* (1999), both at Reynolds numbers comparable to ours. However, it contradicts the picture of vortex merger derived from two-dimensional computations (e.g. Christiansen 1973; Dritschel 1985; Huang 2005; Melander *et al.* 1988) and supported by lower-Reynolds-number experiments (e.g. Meunier *et al.* 2002; Cerretelli & Williamson 2003).

Like all previous data sets quoting core radius, we find a continual increase in this parameter as long as distinct vortices are identifiable. The extent of this increase could possibly be accounted for by a sufficiently large eddy viscosity (as suggested by Cerretelli & Williamson 2003), but its characteristics are not unambiguously diffusive, as the rate of growth appears not to decrease with time. Another potential cause is the artificial increase due to vortex wandering. In Appendix B it is shown that the RMS principal-axis wandering amplitudes, (σ_1,σ_2), are approximately (1.6,0.9) mm and (3.0,1.8) mm at 5 and 13 chords downstream. Following the 'rules of thumb' given by Devenport *et al.* (1996), we correct r_c^2 by $2.51\sigma_w^2$, where $\sigma_w^2 = (\sigma_1^2 + \sigma_2^2)/2$. With reference to figure 5, the core radii of 8.5 mm and 12.5 mm at 0.76 m and 1.98 m reduce to 8.2 mm and 11.9 mm respectively. Although these corrections move the data closer to the turbulent diffusivity curve, one must still postulate a significant (120%) increase in eddy viscosity to attain agreement. This fact, and the qualitative observations of increased unsteadiness as the critical separation is approached, suggest that the elliptic instability also plays a role. At our Reynolds number, the analytical expressions given by Meunier *et al.* (2005) predict that the vortex is linearly unstable throughout the interaction (at least for identical vortices), with growth rate increasing from 3.9 to 6.1 times the inverse orbital period (3.0 to 4.8 times the inverse merger time) as d_0/r_c decreases from 9 to 3.7. During the initial phase of the instability, time-averaged core sizes should be unaffected, but its nonlinear development could well account for the later divergence from the diffusivity curve.

Turning to the most succinct quantitative measure of the merger process, the dimensionless time to merger, we find broad agreement with Chen *et al.*'s value of 0.78 which, as noted earlier, differs significantly from Cerretelli & Williamson's proposed expression for high Reynolds' numbers. However, support for this expression at $Re_\Gamma > 2000$ rests entirely on a single data point from Devenport *et al.* (1999), quoted as 1.31 by Cerretelli & Williamson. Chen *et al* have cast doubt on this value, suggesting that 0.94 is a better estimate. On calculating Devenport *et al.*'s circulation from the amount of rotation seen in their data, we find a comparable value, about 0.8. It thus appears that equal-strength vortices do indeed merge within one initial rotation period. (Note, however, that this does not fully justify the common rule of thumb that such pairs always merge before completing a full rotation, since the rotation rate speeds up as separation decreases; hence the almost $1\frac{1}{2}$ orbits visible pre-merger in figure 4.) The agreement with Chen *et al.* also supports the application of results from vortices generated separately to the more complex wakes behind wings in high-lift configuration.

Our finding that distance to merger decreases as the circulation ratio departs from unity is not easily tested in other data; only Chen *et al.* present results for a significant number of circulation ratios, but their variation is achieved in part by altering the Reynolds number too. Furthermore, their generation method (a flapped wing) precludes the option of producing multiple data points at discrete values of Γ_{01}/Γ_{02}, an approach which, given the scatter in figure 10(*a*), is probably necessary to identify any trends unambiguously. Chen *et al.* do, however, state that vortices of almost equal strength take longer to merge than pairs with differing circulations.

The startling improvement in data collapse when (dimensionless) time to critical separation, instead of merger, is plotted against d_0/r_c requires further discussion. The good collapse supports our 'self-similarity' assumption that each measured location during the progression to merger can be viewed as a new initial condition. Equally, then, the increased scatter in time to merger points to problems with this assumption, which relies on neglecting vortex distortion in the new 'initial' condition. Taken together, these data sets imply that distortion is small and/or has negligible effect during the pre-critical phase, but the ensuing differences in distortion at the critical point lead to significant variations in the remaining time to merger. Certainly the vortices in figure 4 appear almost axisymmetric over most of the initial interaction, but the same cannot be claimed of the unequal pair in figure 8. A more plausible justification is that any distortion of a vortex in the pre-critical phase will have a weak effect on its relatively distant partner, whereas it will become crucially important once vorticity exchange starts around $d_0/r_c = 3.4$. This is an issue that would bear further investigation.

It remains to address the role of three-dimensionality in high-Reynolds-number vortex merger. It is almost certainly always present, via the elliptic instability, during the merger phase. However, the reduction in separation during the pre-merger phase is also crucial, corresponding as it does to a drop in dispersion length that is not permissible in an unconfined two-dimensional incompressible flow, either viscous or inviscid. The occurrence of this feature in Chen *et al.*'s and Devenport *et al.*'s (1999) results suggests that it is not an experimental artefact; however, it is possible that it is somehow due to the confining effect of the wind tunnel walls. We consider this possibility in detail in Appendix A, where we show first that the array of image vorticity fields needed to reproduce the inviscid influence of the walls will leave D unaltered and, second, that viscous effects can only act to decrease it in rather unusual circumstances not found here. Alternatively, a feel for the importance of the former can be obtained by considering the velocity induced by an image with overall circulation $2\,\mathrm{m^2\,s^{-1}}$ at a distance 1.2 m (corresponding to the influence of floor or ceiling). The velocity difference over a typical initial separation of 7 cm (see figure 5) is about $0.015\,\mathrm{m\,s^{-1}}$, which would change the separation by at most 1 mm during the 67 ms that it takes for the vortices to convect 2 m downstream. This upper bound is well below the 20 mm shown in figure 5, without even having taken account of the cancelling effect of other images. Finally, the levelling out of D in figure 6 for $d_0/r_c < 3.4$ is consistent with a switch to purely two-dimensional behaviour once the exchange of vorticity starts, whereas it would not be expected if the earlier decrease were due to confinement effects.

Further evidence of three-dimensional behaviour can be seen in the co-orbiting velocity of the vortices, which can be found by differentiating their angular position with time. This process is prone to introducing noise into the data but it does provide a general trend. In comparison, a pair of purely two-dimensional vortices would co-orbit at the predicted angular velocity used to non-dimensionalize time to merger in equation (3.1). The observed angular velocity is compared to Ω_{pred} throughout the merger process for all the data sets in figure 11. All three data sets collapse onto a similar curve. There appears to be a plateau at large separation where the vortices are co-orbiting at approximately 140% of the predicted velocity. But this enhanced orbital rate tends to deteriorate on approaching the end of the initial interaction phase, at which point the vortices are observed to co-orbit slower than the equivalent two-dimensional case.

We therefore conclude, like Chen *et al.*, that three-dimensionality is significant throughout the merger process at these Reynolds numbers, in spite of the successful collapse onto dimensionless variables inspired by a quasi-two-dimensional analysis. What remains unclear is why such behaviour is not observed at lower Reynolds numbers. It is unlikely that the range of d_0/r_c explored was not large enough, as Cerretelli & Williamson give results up to $d_0/r_c = 8$. However, it is worth noting that none of the experiments they show in their figure 8 have been at sufficiently high both Re_Γ and d_0/r_c to test their predictions for values of dimensionless merger time much greater than unity. It may thus be that three-dimensional effects only become apparent once diffusion would take too long to act.

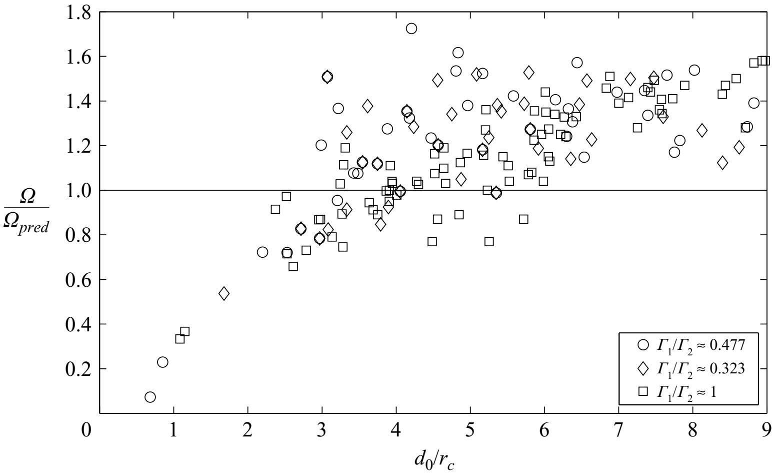

FIGURE 11. Angular velocity normalized by predicted angular velocity as a function of non-dimensionalized separation.

6. Conclusions and summary

Two co-rotating vortices shed from wings generating lift were observed experimentally in a wind tunnel. Downstream crossflow-plane measurements were made for vortices with a range of different initial separations and circulation ratios. The vortices were observed to maintain a circulation profile consistent with the Lamb–Oseen model, even after severe distortion. The early interaction is characterized by the vortices drawing together and growing in radius. Even at the largest initial separation of over 10 core radii the vortices are observed to draw together from formation onwards. Meanwhile, they undergo an increase of core radius not fully consistent with diffusive effects, but maintain their circulation.

The initial interaction phase continues up to the critical separation of $d_0/r_c \approx 3.4$ and is then followed by a vorticity exchange phase. For equal-strength vortices, merger is completed in a convection time of approximately 80% of the initial rotation period, as long as the initial separation-to-radius ratio is above 5. (This result corresponds closely to the findings of Chen *et al.* 1999.) For smaller values of this ratio, merger occurs more rapidly. The corresponding results for unequal-strength vortices show similar asymptotic behaviour, but with a shorter time to merger and more scatter. The latter, however, can be markedly reduced for both unequal and equal vortex cases by plotting (dimensionless) time to critical separation-to-radius ratio instead of to merger.

On the basis of these results, we conclude that the initial interaction, though well-described by a quasi-two-dimensional parameterization, has important three-dimensional aspects. The vorticity exchange phase is presumably responsible for the scatter in (dimensionless) time-to-merger results, and a likely explanation for this is variation in the degree of vortex distortion (caused by the elliptic instability) at the point where this phase starts. However, for high-Reynolds-number flows the 80% estimate for merger time is fairly robust, and appears to apply equally to vortex pairs generated separately and by single wings in high-lift configuration.

The bulk of the work presented in this paper was originally part of a PhD, funded by a Fellowship from the Airworthiness Requirements Board of the UK Civil

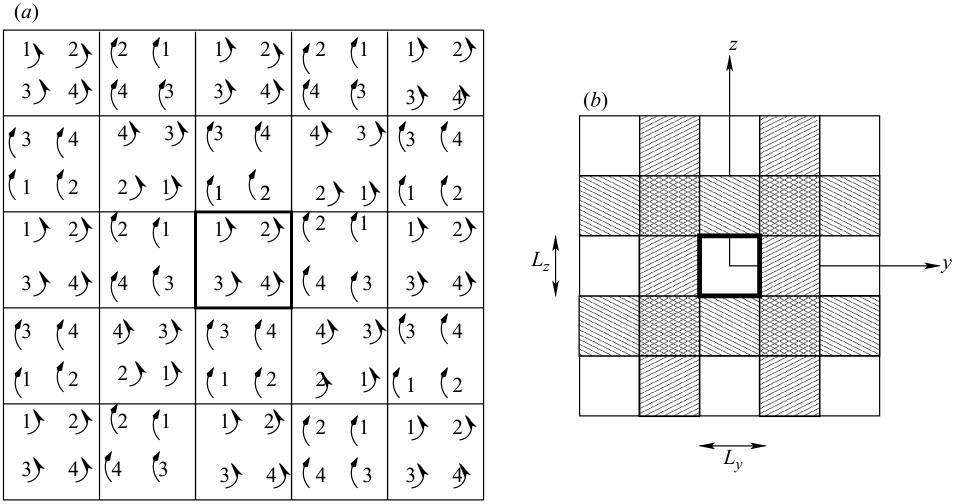

FIGURE 12. Truncated 5 × 5 array of image flows representing the effect of wall confinement: (*a*) schematic of real and image vorticity fields; (*b*) diagram showing repeat pattern. Note that the origin of coordinates is now placed at the centre of the wind tunnel cross-section.

Aviation Authority (CAA). The authors gratefully acknowledge the support of the CAA's project manager, Steve Griffin, and technical consultant, Alan Woodfield. We would also like to thank our referees, whose awkward questions led to significant improvements on the initial version.

Appendix A. The effect of flow confinement on dispersion length

Here we investigate whether the confinement of a two-dimensional flow could lead to the decrease in dispersion length observed in our experiments. We consider first, in § A1, the inviscid case, and then address the contribution of viscous effects in § A2.

A.1. *Invariants of a confined, two-dimensional inviscid flow*

The normal velocity boundary condition at the walls of a confined flow may be enforced via the use of image flow fields. In the case of our rectangular wind tunnel cross-section, of width L_y and height L_z, the required array of image velocity fields is shown schematically in figure 12. In principle, the images extend to infinity, but here we observe that arbitrary accuracy may be attained with a large, but finite, set. In addition, our chosen array has equal numbers of 'cells' in the horizontal and vertical directions, and equal numbers either side of the real flow field.

The vorticity field of our array is given by

$$\begin{aligned} \omega_x(y+iL_y, z+jL_z) &= \omega_x(y,z), && i, j \text{ even}, \\ &= -\omega_x(L_y-y, z), && i \text{ odd}, j \text{ even}, \\ &= -\omega_x(y, L_z-z), && i \text{ even}, j \text{ odd}, \\ &= \omega_x(L_y-y, L_z-z), && i, j \text{ odd}, \end{aligned} \qquad \text{(A 1)}$$

with $-L_y/2 \leqslant y \leqslant L_y/2$, $-L_z/2 \leqslant z \leqslant L_z/2$. Its circulation $\Gamma_a = \iint \omega \, \mathrm{d}y \, \mathrm{d}z$ is given by the summation of the individual cells' circulations:

$$\Gamma_a = \sum_{i,j} \Gamma_{ij} \qquad \text{(A 2)}$$

where $\Gamma_{ij} = (-1)^{i+j}\Gamma$, with

$$\Gamma = \int_{-L_z/2}^{L_z/2} \int_{-L_y/2}^{L_y/2} \omega(y, z)\, \mathrm{d}y\, \mathrm{d}z.$$

On starting the summation (A 2) at our central cell (the real flow), and then proceeding over concentric rectangles of cells, we find that $\Gamma_a = \Gamma$. Now the circulation of the unconfined array is invariant (see, for example, Batchelor 1967), as, therefore, is the circulation Γ of our confined flow. This result could, of course, have been obtained more straightforwardly via Kelvin's circulation theorem, but has been derived in this way to illustrate the method, which can now also be applied to the centroid of vorticity and the dispersion length.

The spanwise location of the array's vorticity centroid follows from equations (2.2) and (A 1) as

$$\overline{Y}_a = \sum_{i,j} (-1)^{i+j} [i L_y + \overline{y}_{ij}],$$

where $\overline{y}_{ij}$ is the spanwise centroid position of the (i, j)th cell, in local coordinates (i.e. relative to the cell centre). It is given by

$$\begin{aligned} \overline{y}_{ij} &= \overline{Y}, & i \text{ even}, \\ \overline{y}_{ij} &= L_y - \overline{Y}, & i \text{ odd}. \end{aligned}$$

A similar result applies to the vertical centroid coordinate. The only non-constant terms on which the array centroid location depends are thus the real flow centroid coordinates, $\overline{Y}$ and $\overline{Z}$, so the invariance of the array centroid (Batchelor 1967) implies that the centroid of the confined flow is similarly fixed.

Finally, the dispersion length of the array can be calculated from the integral $\int\int \omega_x (y^2 + z^2)\, \mathrm{d}y\, \mathrm{d}z$ over all the images, which yields

$$\begin{aligned} D_a^2 + \overline{Y}_a^2 + \overline{Z}_a^2 = \sum_{i,j} (-1)^{i+j} \{ & (i L_y)^2 + (j L_z)^2 + 2 i L_y \overline{y}_{ij} \\ & + 2 j L_z \overline{z}_{ij} + D^2 + \overline{y}_{ij}^2 + \overline{z}_{ij}^2 \}. \end{aligned}$$

Again, the unbounded result that D_a is invariant (Batchelor 1967) implies also that the dispersion length of our confined flow remains constant.

A.2. *The influence of viscosity*

Once viscous effects are included, the flow is governed by the two-dimensional Navier–Stokes equations, whose invariants in the absence of boundaries are considered by Dritschel (1985). It is straightforward to apply the same analysis to the bounded case, with identical results (namely, that circulation and centroid location are invariant, and dispersion length increases at a rate $2\nu/D$) as long as there is negligible vorticity on the enclosing contour. The existence of a boundary satisfying this condition is strongly supported by the contour plots of figures 4 and 8; quantitative corroboration comes from the constancy of our estimated circulation. We therefore conclude that a reduction in dispersion length due to viscous effects requires conditions not present in our experiment.

Appendix B. Approximate characterization of vortex wandering

B.1. *Approach*

A fully accurate characterization of wandering requires time-resolved measurements of all three velocity components (Devenport *et al.* 1996). Such an approach was beyond the scope of the present study, and an alternative method, applicable to single-hot-wire data, was therefore developed.

We note, first, that the degree of wandering deduced from Devenport *et al.*'s (1999) measurements of a co-rotating pair is essentially the same as that found for a single vortex in the same facility (Devenport *et al.* 1996). Furthermore, a hot-wire oriented azimuthally in a single, steady vortex will respond to the streamwise velocity component only. We therefore base our method on single-wire measurements behind one of the vortex-generating wings. The streamwise velocity mean and RMS fluctuation are characterized by two line traverses through the vortex: one horizontal (with the wire vertical) and one vertical (with the wire horizontal). The hot-wire output is anti-alias filtered at 500 Hz and sampled at 1200 Hz, for 150s. The formulation for the deduction of wandering amplitudes from these data is presented in the following section. The results, at streamwise locations 5 and 13 chords behind the wing, are given in § B.3.

B.2. *Formulation*

The ability of the azimuthally oriented hot wire to reject both crossflow velocity components must first be examined more carefully. For example, on the vertical traverse with horizontal wire, the measured velocity will actually be

$$q = \sqrt{(U+u)^2 + w^2}, \tag{B 1}$$

where u and w are the x- and z-wise departures from the free stream, the latter arising solely due to the wandering of the vortex. However, as long as $u/U,\ w/U \ll 1$, one has

$$\overline{q} \approx U + \overline{u} + \frac{1}{2}\frac{\overline{w^2}}{U} \tag{B 2}$$

and

$$\overline{q^2} - \overline{q}^2 \approx \overline{(u-\overline{u})^2}, \tag{B 3}$$

where the overbars denote average values. The mean and RMS fluctuation of the hot-wire measurements are thus expected to provide good approximations to the corresponding properties of the streamwise velocity.

Preliminary inspection of the fluctuation spectra near the vortex core showed that RMS levels here were almost entirely due to low-frequency components (below 50 Hz), and were thus dominated by wandering contributions. Devenport *et al.* (1996) have pointed out that Gaussian wandering can lead to a measured Gaussian structure, even if the underlying vortex is not Gaussian. In spite of this caveat, we restrict consideration to a vortex with a streamwise velocity excess given by

$$u(y-y_c, z-z_c) = U_J \exp\left[-\frac{(y-y_c)^2 + (z-z_c)^2}{\sigma^2}\right], \tag{B 4}$$

where (y_c, z_c) are the vortex centre coordinates, and σ is the (axial) core length scale. Then (Devenport *et al.* 1996) the average measured excess is

$$\overline{u}_m(y,z) = \int\!\!\int u(y-y_c, z-z_c)\, p(y_c, z_c)\, \mathrm{d}y_c\, \mathrm{d}z_c, \tag{B 5}$$

where $p(y_c, z_c)$ is the probability density function of the wandering. Anisotropic Gaussian wandering corresponds to

$$p(y_c, z_c) = \frac{1}{2\pi\sigma_1\sigma_2}\exp\left[-\frac{Y_c^2}{2\sigma_1^2} - \frac{Z_c^2}{2\sigma_2^2}\right], \tag{B 6}$$

with σ_1, σ_2 the RMS wandering amplitudes in the principal axis directions Y_c, Z_c. The latter are centred on the mean vortex position and rotated through an angle ϕ, i.e.

$$Y_c = (y_c - \overline{y}_c)\cos\phi + (z_c - \overline{z}_c)\sin\phi, \tag{B 7}$$

$$Z_c = -(y_c - \overline{y}_c)\sin\phi + (z_c - \overline{z}_c)\cos\phi. \tag{B 8}$$

Equation (B 5) is straightforward to evaluate analytically. In particular, for the horizontal and vertical traverses, we find

$$\overline{u}_m(y, \overline{z}_c) = \frac{U_J\sigma^2}{\sqrt{(\sigma^2 + 2\sigma_1^2)(\sigma^2 + 2\sigma_2^2)}}\exp\left[-\frac{(y - \overline{y}_c)^2}{\sigma^2 + 2\sigma_1^2}\cos^2\phi - \frac{(y - \overline{y}_c)^2}{\sigma^2 + 2\sigma_2^2}\sin^2\phi\right] \tag{B 9}$$

and

$$\overline{u}_m(\overline{y}_c, z) = \frac{U_J\sigma^2}{\sqrt{(\sigma^2 + 2\sigma_1^2)(\sigma^2 + 2\sigma_2^2)}}\exp\left[-\frac{(z - \overline{z}_c)^2}{\sigma^2 + 2\sigma_1^2}\sin^2\phi - \frac{(z - \overline{z}_c)^2}{\sigma^2 + 2\sigma_2^2}\cos^2\phi\right]. \tag{B 10}$$

For $\sigma_1 = \sigma_2$, these expressions reduce to the isotropic wandering result given by Devenport *et al.* (1996).

The RMS streamwise velocity fluctuation can be written solely in terms of the velocity excess:

$$u_{rms} = \sqrt{\overline{u_m^2} - \overline{u}_m^2}. \tag{B 11}$$

Here $\overline{u_m^2}$ is derived in identical manner to $\overline{u}_m$. When the integral corresponding to (B 5) is evaluated, we find

$$\overline{u_m^2}(y, \overline{z}_c) = \frac{U_J^2\sigma^2}{\sqrt{(\sigma^2 + 4\sigma_1^2)(\sigma^2 + 4\sigma_2^2)}}\exp\left[-\frac{2(y - \overline{y}_c)^2}{\sigma^2 + 4\sigma_1^2}\cos^2\phi - \frac{2(y - \overline{y}_c)^2}{\sigma^2 + 4\sigma_2^2}\sin^2\phi\right] \tag{B 12}$$

and

$$\overline{u_m^2}(\overline{y}_c, z) = \frac{U_J^2\sigma^2}{\sqrt{(\sigma^2 + 4\sigma_1^2)(\sigma^2 + 4\sigma_2^2)}}\exp\left[-\frac{2(z - \overline{z}_c)^2}{\sigma^2 + 4\sigma_1^2}\sin^2\phi - \frac{2(z - \overline{z}_c)^2}{\sigma^2 + 4\sigma_2^2}\cos^2\phi\right]. \tag{B 13}$$

Equations (B 9), (B 10), (B 12) and (B 13) form the basis of the wandering-amplitude estimation method. This has two parts: first the measured mean velocities are fitted to Gaussian profiles, and then the measured RMS velocities are fitted to (B 11), using either (B 9) and (B 12) or (B 10) and (B 13) for its component terms. A proprietary nonlinear least-squares routine is used for these calculations.

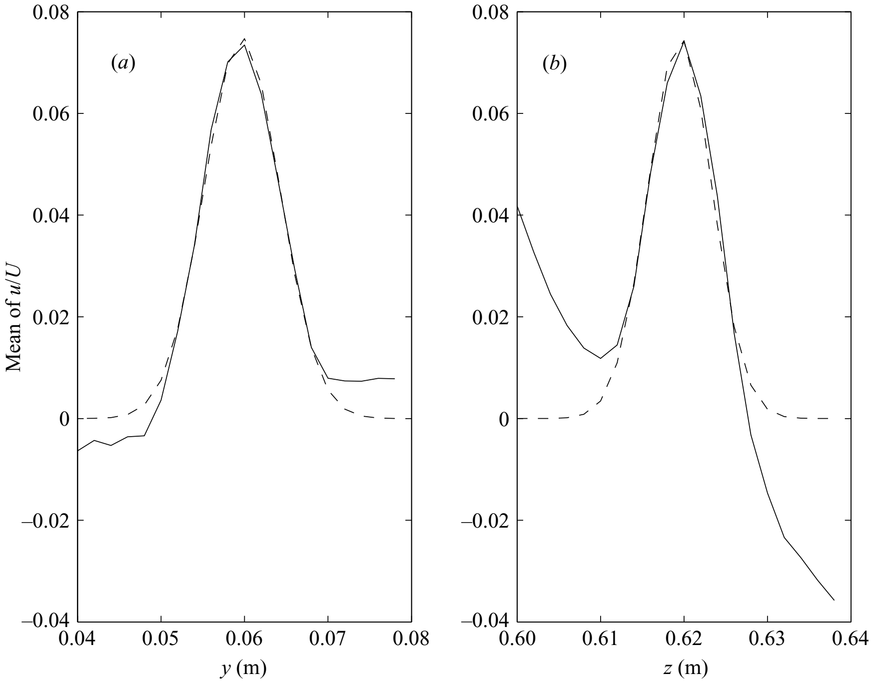

FIGURE 13. Measured (—) and fitted (- - -) mean velocities: (*a*) horizontal traverse, with best-fit parameters $\overline{y}_c = 0.060\,\mathrm{m}$, $U = 27.0\,\mathrm{m\,s^{-1}}$, $\tilde{U}_{Jm} = 0.075$, $r_y = 0.0064\,\mathrm{m}$; (*b*) vertical traverse, with best-fit parameters $\overline{z}_c = 0.620\,\mathrm{m}$, $U = 29.0\,\mathrm{m\,s^{-1}}$, $\tilde{U}_{Jm} = 0.075$, $r_z = 0.0054\,\mathrm{m}$.

The mean velocity profiles yield the best-fit parameters $\tilde{U}_{Jm}$, r_y and r_z, where

$$\tilde{U}_{Jm} = \frac{U_J}{U}\frac{\sigma^2}{\sqrt{\left(\sigma^2 + 2\sigma_1^2\right)\left(\sigma^2 + 2\sigma_2^2\right)}}, \tag{B 14}$$

$$\frac{1}{r_y^2} = \frac{\cos^2\phi}{\sigma^2 + 2\sigma_1^2} + \frac{\sin^2\phi}{\sigma^2 + 2\sigma_2^2}, \tag{B 15}$$

$$\frac{1}{r_z^2} = \frac{\sin^2\phi}{\sigma^2 + 2\sigma_1^2} + \frac{\cos^2\phi}{\sigma^2 + 2\sigma_2^2}. \tag{B 16}$$

The parameters U, $\overline{y}_c$ and $\overline{z}_c$ are also derived from this process, rather than specified in advance. Interpolation between several linear traverses is employed to derive an estimated measured profile at the required value of $\overline{y}_c$ (for vertical traverses) or $\overline{z}_c$ (for horizontal traverses). As $\overline{y}_c$ and $\overline{z}_c$ are not known exactly in advance, one or two manual iterations are necessary, but convergence is rapid.

The RMS velocity profiles are then used to find the best-fit values for U_J/U, σ, σ_1, σ_2 and ϕ, subject to the constraints (B 14)–(B 16). In practice, this is achieved by allowing the parameters σ_1 and σ_2 to vary, with the corresponding values of the remaining terms found by solving (B 15), (B 16) for σ, ϕ, and then (B 14).

B.3. *Results*

Figure 13 shows the measured and fitted mean velocity profiles for both horizontal and vertical traverses at 13 chords downstream. The corresponding parameter values

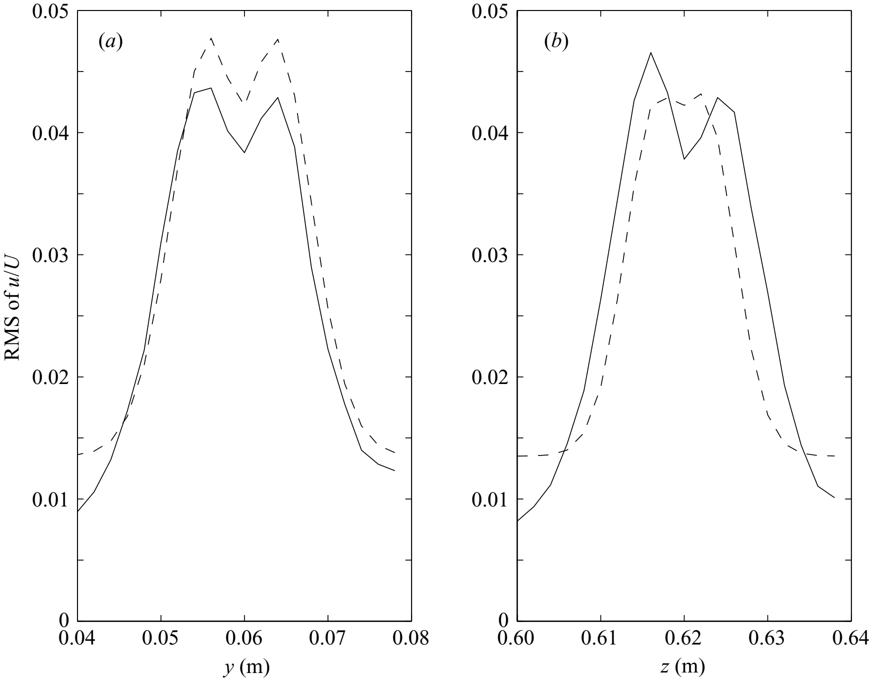

FIGURE 14. Measured (—) and fitted (- - -) RMS velocities: (*a*) horizontal traverse; (*b*) vertical traverse. Best-fit parameters $\sigma_1 = 0.0030$ m, $\sigma_2 = 0.0018$ m, background level $0.014U$. Constrained parameters $(U_J/U) = 0.114$, $\sigma = 0.0048$, $\phi = 2.6°$.

Downstream distance	σ_1 (m)	σ_2 (m)	ϕ (deg.)
$5c$	0.0016	0.0009	9.4
$13c$	0.0030	0.0018	2.6

TABLE 1. Estimated wandering parameters

are given in the caption. Although the vertical traverse measurements exhibit some asymmetry, perhaps due to the wing wake, the data generally show a good match to Gaussian profiles.

Figure 14 shows the corresponding results for the RMS velocities. (Note that a background level has been included in the fit.) Here the detailed comparison between the theoretical forms and the data is less good. The overall topology is, however, sufficiently similar to support the form assumed for the axial velocity, and the use of single hot-wire measurements to obtain this quantity. The derived values are approximately twice those found by Devenport *et al.* (1996) at the same downstream location.

The analysis for the measurements taken 5 chords downstream proceeds identically, and shows similar levels of agreement. The wandering parameters for both downstream stations are summarized in table 1.

REFERENCES

Anderson, E. A., Snyder, D. O., Wright, C. T. & Spall, R. E. 2001 Numerical/experimental investigation into multiple vortex structures formed over wings with flat end-caps. *AIAA Paper* 2001-0112.

Batchelor, G. K. 1967 *An Introduction to Fluid Dynamics*. Cambridge University Press.

Bertényi, T. 2001 Merger of aircraft wake vortices. PhD thesis, University of Cambridge.

Brandt, S. A. & Iversen, J. D. 1977 Merging of aircraft trailing vortices. *J. Aircraft* **14**, 1212–1220.

Bristol, R. L., Ortega, J. M., Marcus, P. S. & Savaş, Ö 2004 On cooperative instabilities of parallel vortex pairs. *J. Fluid Mech.* **517**, 331–358.

Bristol, R. L., Ortega, J. M. & Savaş, Ö 2003 Experimental study of corotating wake-vortex merger at Reynolds numbers of order 10^5. *AIAA J.* **41**, 741–744.

Burnham, D. C. & Sullivan, T. E. 1973 Influence of flaps and engines on aircraft wake vortices. *J. Aircraft* **11**, 591–592.

Cerretelli, C. & Williamson, C. H. K. 2003 The physical mechanism for vortex merging. *J. Fluid Mech.* **475**, 41–77.

Chen, A. L., Jacob, J. D. & Savas, O. 1999 Dynamics of corotating vortex pairs in the wakes of flapped airfoils. *J. Fluid Mech.* **382**, 155–193.

Christiansen, J. P. 1973 Numerical simulation of hydrodynamics by method of point vortices. *J. Comput. Phys.* **13**, 363–379.

Chu, J. K., Rios-Chiquete, E., Sarohia, S., & Bernstein, L. 1987 The ’Chu-Tube’: a velocimeter for use in highly-sheared, three-dimensional steady flows. *Aero. J.* **March**, 142–149.

Corsiglia, V. R., Rossow, V. J. & Ciffone, D. L. 1976 Experimental study of the effect of span loading on aircraft wakes. *J. Aircraft* **13**, 968–973.

Crouch, J. 2005 Airplane trailing vortices and their control. *C. R. Physique* **6**, 487–499.

Czech, M., Miller, G., Crouch, J. & Strelets, M. 2005 Predicting the near-field evolution of airplane trailing vortices. *C. R. Physique* **6**, 451–466.

Dacles-Mariani, J., Zilliac, G. G., Chow, J. S. & Bradshaw, P. 1995 Numerical/experimental study of a wingtip vortex in the near field. *AIAA J.* **33**, 1561–1568.

Devenport, W. J., Rife, M. C., Liapis, S. I. & Follin, G.J. 1996 The structure and development of a wing-tip vortex. *J. Fluid Mech.* **312**, 67–106.

Devenport, W. J., Vogel, C. M. & Zsoldos, J. S. 1999 Flow structure produced by the interaction and merger of a pair of co-rotating wing-tip vortices. *J. Fluid Mech.* **394**, 357–377.

Dritschel, D. G. 1985 The stability and energetics of corotating uniform vortices. *J. Fluid Mech.* **157**, 95–134.

Dritschel, D. G. & Waugh, D. W. 1992 Quantification of the inelastic interaction of unequal vortices in two-dimensional vortex dynamics. *Phys. Fluids* A **4**, 1737–1744.

Gardoz, L. J. & Clawson, K. L. 1993 Vortex wake characteristics of B757-200 and B767-200 Aircraft. *ERL ARL-199* **1,2**.

Graham, W. R., David, L. & Bertényi, T. 2004 The effect of flap-end additions on aircraft trailing vortices. *Aero. J.* **February**, 109–115.

Green, S. I. & Acosta, A. J. 1991 Unsteady flow in trailing vortices. *J. Fluid Mech.* **227**, 107–134.

Huang, M.-J. 2005 The physical mechanism of symmetric vortex merger: A new viewpoint *Phys. Fluids* **17**, 074105.

Iversen, J. D. 1976 Correlation of turbulent trailing vortex decay data. *J. Aircraft* **13**, 338–342.

Iversen, J. D., Corsiglia, V. R., Park, S., Backhus, D. R. & Brickman, R. A. 1979 Hot-wire, laser-anemometer, and force measurements of interacting trailing vortices. *J. Aircraft* **16**, 448–454.

Jacquin, L., Fabre, D., Sipp, D. & Coustols, E. 2005 Unsteadiness, instability and turbulence in trailing vortices *C. R. Physique* **6**, 399–414.

Jimenez, J., Moffatt, H. K. & Vasco, C. 1996 The structure of vortices in freely decaying two-dimensional turbulence. *J. Fluid Mech.* **313**, 209–222.

Le Dizès, S. & Laporte, F. 2002 Theoretical predictions for the elliptical instability in a two-vortex flow *J. Fluid Mech.* **471**, 169–201.

Melander, M. V., Zabusky, N. J. & McWilliams, J. C. 1988 Symmetric vortex merger in two dimensions: causes and conditions. *J. Fluid Mech.* **195**, 303–340.

Meunier, P., Ehrenstein, U., Leweke, T. & Rossi, M. 2002 A merging criterion for two-dimensional co-rotating vortices. *Phys. Fluids* **14**, 2757–2766.

Meunier, P., Le Dizès, S. & Leweke, T. 2005 Physics of vortex merging. *C. R. Physique* **6**, 431–450.

Meunier, P., & Leweke, T. 2005 Elliptic instability of a co-rotating vortex pair. *J Fluid Mech.* **533**, 125–159.

Ramaprian, B. R. & Zheng, Y. 1997 Measurements in rollup region of the tip vortex from a rectangular wing. *AIAA J.* **35**, 1837–1843.

Roberts, C. L., Vicroy, D. D. & Smith, S. T. 2000 Flight test analysis of the forces and moments imparted on a B737-100 aircraft during wake vortex encounters. *AIAA Paper* 2000–3908.

Rossow, V. J. 1977 Convective merging of vortex cores in lift-generated wakes. *J. Aircraft* **14**, 283–290.

Rossow, V. J. 1999 Lift-generated vortex wakes of subsonic transport aircraft. *Prog. Aerospace Sci.* **6**, 507–660.

Saffman, P. G. 1992 *Vortex Dynamics*. Cambridge University Press.

Spalart, P. R. 1998 Airplane trailing vortices. *Annu. Rev. Fluid Mech.* **30**, 107–138.

Spall, R. E. 2001 Numerical study of a wing-tip vortex using the Euler equations. *J. Aircraft* **38**, 22–27.

Trieling, R. R., Velasco Fuentes, O. U. & van Heijst, G. J. F. 2005 Interaction of two unequal corotating vortices. *Phys. Fluids* **17**, 087103.